High-T_c superconductivity in squeezed cubic $CSeH_6$ and C_2TeH_8 ternary polyhydrides

Shoutao Zhang,[1,*] Hong Yu,[1] Jiahui Wei,[1] Ting Zhong,[1] Jiance Sun,[1] Qianyi Wang,[1] Lulu Liu,[2] Haiyang Xu,[1] Jiangang Ma,[1] and Hanyu Liu[3,†]

[1]*Key Laboratory of UV-Emitting Materials and Technology of Ministry of Education, School of Physics, Northeast Normal University, Changchun 130024, China*

[2]*School of Electronic Engineering, Nanjing Xiaozhuang University, Nanjing 211171, China*

[3]*Key Laboratory of Material Simulation Methods and Software of Ministry of Education and State Key Laboratory of Superhard Materials, College of Physics, Jilin University, Changchun 130012, China*

(Received 25 January 2024; accepted 10 April 2024; published 3 May 2024)

The recent discovery of high-temperature superconductivity in hydrogen-based compounds under pressure has fueled the hope for the exploration of hydrides with high critical temperatures (T_c). In this work, we systematically investigated pressure-stabilized ternary C-Se-H and C-Te-H compounds using the state-of-the-art structure prediction approach in combination with first-principles calculations. As a result, our simulations identified two cubic phases ($CSeH_6$ and C_2TeH_8) with a metastable stability feature. Fd-3m-structured $CSeH_6$ adopted a diamond-type host Se framework with an embedded guest CH_6 covalent octahedron, and C_2TeH_8 with Fm-3m symmetry adopted a face-centered cubic arrangement of H_8 cubes, which are interlinked by a molecular unit CH_4 tetrahedron. Electron-phonon coupling simulations reveal that $CSeH_6$ has high-temperature superconductivity with a T_c of 80.6 K at 250 GPa. This high superconductivity could be attributed to the fact that the C 2p, Se 4p, and H 1s electron states near the Fermi energy couple with high-frequency H-associated phonons. Furthermore, C_2TeH_8 was estimated to have an even higher T_c of 151.4 K at 300 GPa due to the large average phonon frequency and the strong coupling between C- and H-derived optical phonons and electrons (C 2p, Te 5p, and H 1s) near the Fermi level. The present results shed light on the future exploration of high-temperature superconductivity among multinary hydrides.

DOI: 10.1103/PhysRevB.109.174507

I. INTRODUCTION

The exploration of high-temperature or room-temperature superconducting materials remains a hot topic in the fields of condensed matter physics, chemistry, and materials science [1–5]. Hydrogen-rich compounds were considered as a typical class of conventional Bardeen-Cooper-Schrieffer superconductors and have received much interest in recent decades for their peculiar hydrogen structures, high superconductivity, as well as their low metallization pressure compared to atomic metallic hydrogen [6–9]. Binary hydrides were discovered to have high-temperature superconductivity, where there are two typical classes of superconductors [10–12]. One includes hydrides with covalent bonds between hydrogen and other light nonmetal elements. For example, high-T_c sulfur hydrides (SH_3) were theoretically predicted [13,14] and subsequently verified by an experimental study [15]. The other one is clathrate-like superhydrides containing alkaline and rare-earth metals [16–19], e.g., predicted high-T_c superconductive phases CaH_6 (210–215 K at 160–172 GPa) [20,21] and LaH_{10} (250–260 K at 170–188 GPa) [22,23] were successfully synthesized.

Recently, as a unique material platform, ternary hydrides with more complex chemical space have attracted much attention because of their diverse structures and high-T_c superconductivity [24–28]. These ternary hydrides can be categorized into three main groups (see the Appendix): ternary hydrogen-based metal-free compounds [29–31], ternary hydrogen-based compounds with one type of metal element [32–39], and one with two types of metal elements [40–48]. Very recently, $LaBeH_8$ with a rocksalt-like structure [49] was successfully synthesized [50], exhibiting high-T_c superconductivity up to 110 K at 80 GPa. These findings greatly encourage a further search for high superconductivity in ternary hydrides.

Metastable hydrides also hold intriguing hydrogen motifs and promising high superconductivity [51–60]. For example, the predicted cubic Li_2MgH_{16} has a cagelike hydrogen sublattice and a remarkable T_c of 473 K at 250 GPa [61]. Hexagonal HfH_{10} with a hydrogen pentagon-like structure was predicted to exhibit high-T_c superconductivity with 213–234 K at 250 GPa [62]. (La, Al)H_{10} with $P6_3/mmc$ symmetry was recently synthesized by introducing Al into metastable hexagonal LaH_{10} and had an observed T_c of 223 K at 164 GPa [63]. A cubic metastable hydride superconductor, Mg_2IrH_6, was predicted to have a high T_c of 160 K at ambient pressure [64].

Several ternary carbon-sulfur-hydrogen compounds were recently reported to show highly promising superconductivity [65–69], such as $C_2S_3H_4$ (47.4 K at 300 GPa) [70], $CH_{10}S_2$ (125 K at 300 GPa) [71], metastable CSH_{48} with

*Corresponding author: zhangst966@nenu.edu.cn
†Corresponding author: hanyuliu@jlu.edu.cn

H_2 units (156 K at 300 GPa) [72], and low-level carbon-doped $H_3S_{0.917}C_{0.083}$ (189 K at 300 GPa) [72]. It is well known that selenium (Se) and tellurium (Te) are isoelectronic to S and exhibit similar physical properties to S [73–78]. Meanwhile, high superconductivity was predicted in compressed hydrogen-rich H-Se [79–82] and H-Te [83] compounds. Therefore, the study of ternary C-Se and C-Te hydrides with interesting structural motifs and high-temperature superconductivity at pressure remains required.

In this work, we investigated the hydrogen-rich phases in the C-Se-H and C-Te-H ternary systems at compression conditions using the first-principles structure search method. Interestingly, two metastable multihydrogen $CSeH_6$ and C_2TeH_8 phases with both cubic symmetry and metallic characteristics were identified. Meanwhile, a diamond-type Se arrangement and a H_8 cube were found in Fd-3m $CSeH_6$ and Fm-3m C_2TeH_8, respectively. Electron-phonon coupling calculations suggested that Fd-3m-structured $CSeH_6$ had a high-T_c superconductivity of 80.6 K at 250 GPa. Furthermore, C_2TeH_8 in the Fm-3m structure exhibited a higher T_c of 151.4 K at 300 GPa.

II. COMPUTATIONAL DETAILS

In order to obtain ternary C-Se-H and C-Te-H compounds with high superconductivity, we focused on the structure prediction of C-Se-H and C-Te-H systems with the hydrogen-rich compositions under pressure through the CALYPSO software package [84,85], which was able to design stable or metastable materials [86–90]. Structural optimization and electronic properties were achieved through the Vienna *ab initio* simulation package (VASP) code [91]. Projector augmented wave (PAW) [92] pseudopotentials with following valence electrons of $2s^2\,2p^2$ for C, $4s^2\,4p^4$ for Se, $5s^2\,5p^4$ for Te, and $1s^1$ for H were selected. The validity of the adopted PAW pseudopotentials under compression has been corroborated by previous works for binary C-H [93], Se-H [79], and Te-H [83] compounds. The exchange-correlation interactions were described by the Perdew-Burke-Ernzerhof [94] functional within the generalized gradient approximation [95]. A kinetic energy cutoff of 800 eV for plane-wave expansion and a k-grid sampling [96] with a spacing of $2\pi \times 0.02$ Å^{-1} in reciprocal space were employed to assure the convergence of the total energies. Phonon dispersion curves were calculated by PHONOPY software [97]. The QUANTUM ESPRESSO package [98] was used to implement the calculations of superconductive properties. The superconductive transition temperature T_c was calculated using the Allen-Dynes modified McMillan formula [99,100]:

$$T_c = f_1 f_2 \frac{\omega_{\log}}{1.2} \exp\left(\frac{-1.04(1+\lambda)}{\lambda - \mu^*(1+0.62\lambda)}\right). \quad (1)$$

$$f_1 = \left[1 + \left(\frac{\lambda}{2.46(1+3.8\mu^*)}\right)^{3/2}\right]^{1/3}, \quad (2)$$

$$f_2 = 1 + \frac{\left(\frac{\bar{\omega}}{\omega_{\log}} - 1\right)\lambda^2}{\lambda^2 + \left[1.82(1+6.3\mu^*)\frac{\bar{\omega}}{\omega_{\log}}\right]^2}, \quad (3)$$

$$\bar{\omega} = \langle \omega^2 \rangle^{1/2}. \quad (4)$$

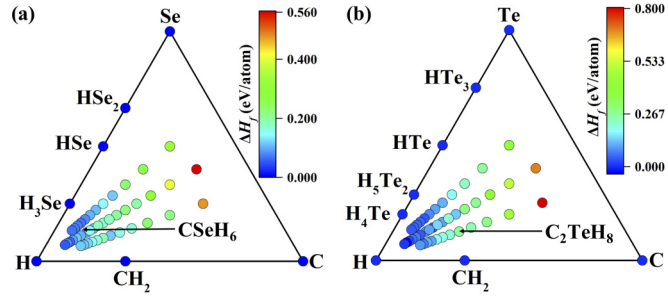

FIG. 1. Phase diagram of (a) C-Se-H and (b) C-Te-H ternary systems at 300 GPa. The blue circles on the side of the triangle denote the thermodynamically stable phases. The circles of different colors in the triangle indicate the metastable phases. Different color scales indicate the magnitude of the formation enthalpies per atom of $C_xSe_yH_z$ or $C_xTe_yH_z$ structures with respect to elementary C, Se/Te, and H substances.

Here, the strong-coupling f_1 and shape correction f_2 factors are included. Coulomb repulsion pseudopotentials μ^* with widely accepted values of 0.10 and 0.13 are adopted. The electron-phonon coupling (EPC) parameter λ and the logarithmic average phonon frequency $\omega_{\log}$ were computed as

$$\lambda(\omega) = 2\int_0^\infty \frac{\alpha^2 F(\omega)}{\omega} d\omega, \quad (5)$$

$$\omega_{\log} = \exp\left[\frac{2}{\lambda}\int_0^\infty \frac{d\omega}{\omega}\alpha^2 F(\omega)\ln(\omega)\right]. \quad (6)$$

More details of the calculations are depicted in the Supplemental Material [101] (see also Refs. [102,103] therein).

III. RESULTS AND DISCUSSION

A. Phase stability of ternary C-Se-H and C-Te-H systems

We began our simulations on the structure search of the hydrogen-rich $C_xSe_yH_z$ ($x = 1-2$, $y = 1-2$, $z = 1-12$) and $C_xTe_yH_z$ ($x = 1-2$, $y = 1-2$, $z = 1-12$) compounds. The size of the simulation cell was up to 4 formula units (f.u.), and the selected pressure was 300 GPa. Then, each $C_xSe_yH_z$ or $C_xTe_yH_z$ configuration with the lowest enthalpy was selected to compute the formation enthalpy ΔH_f per atom related to elementary substances C, Se/Te, and H. Ternary phase diagrams of the C-Se-H and C-Te-H systems at 300 GPa were established from the ΔH_f values to examine the energetic stabilities of the $C_xSe_yH_z$ and $C_xTe_yH_z$ phases, respectively (Fig. 1). Meanwhile, we reproduced the stabilities of binary CH_2 [93], HSe_2 [79], HSe [79], H_3Se [79], HTe_3 [83], HTe [83], H_5Te_2 [83], and H_4Te [83] structures by calculating their formation enthalpies with respect to the constituent elements. As illustrated in Fig. 1, all studied $C_xSe_yH_z$ or $C_xTe_yH_z$ compounds were thermodynamically unstable relative to elemental solids, but they can be considered as metastable phases. Some materials synthesized under high pressure and high temperature are metastable, including nitrogen allotropes [104,105] and diamond [106]. Here, ternary hydrides $CSeH_6$ with Fd-3m symmetry and C_2TeH_8 with space group Fm-3m were used as examples (Fig. 1). The lowest formation enthalpies for Fd-3m $CSeH_6$ and Fm-3m C_2TeH_8 were 101.4

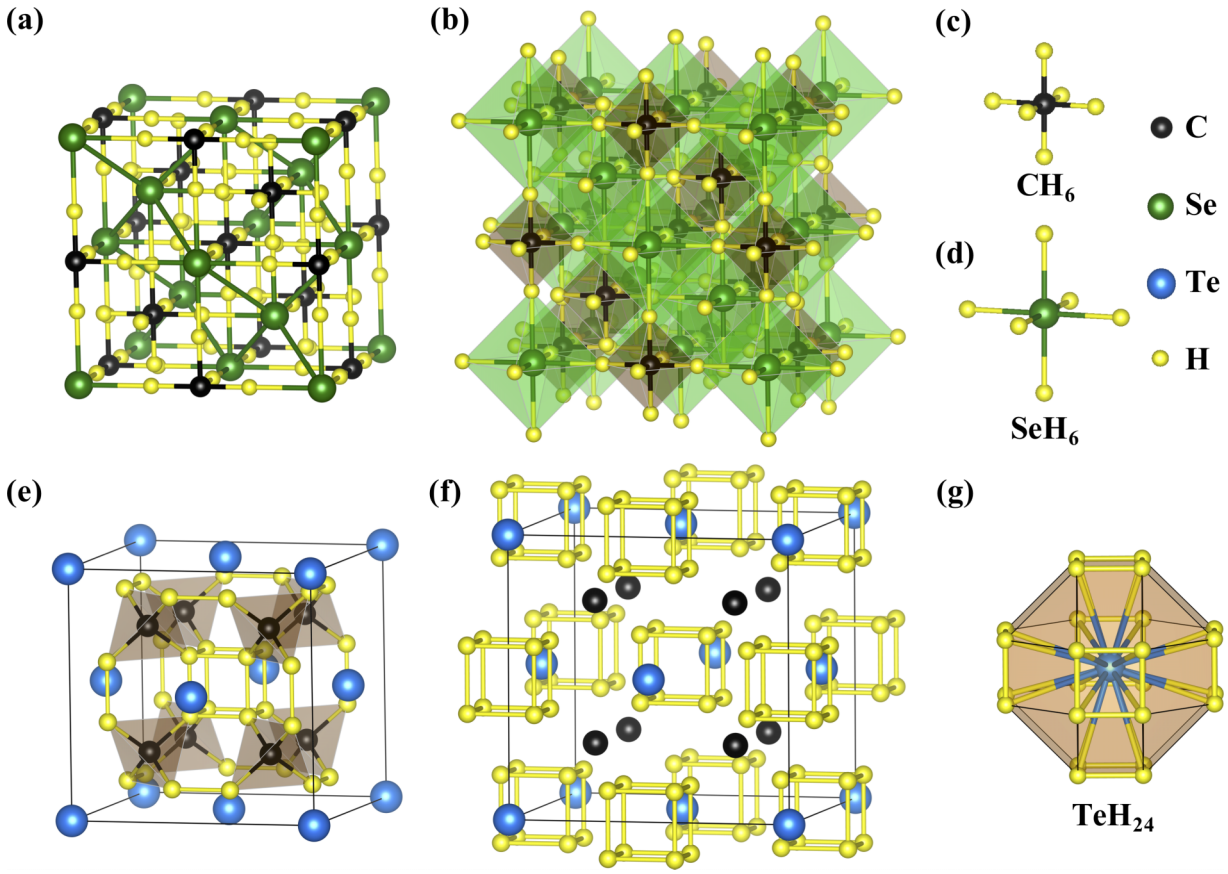

FIG. 2. Crystal structures of the predicted metastable Fd-3m $CSeH_6$ and Fm-3m C_2TeH_8 phases at 300 GPa. (a) $CSeH_6$ with a diamondlike Se configuration. (b) CH_6 and SeH_6 octahedra in $CSeH_6$. (c) Sixfold coordination of C in $CSeH_6$. (d) Sixfold coordination of Se in $CSeH_6$. (e) C_2TeH_8 containing tetrahedral CH_4 and cubic H_8 units. (f) H_8 cubes with the face-centered cubic arrangement in C_2TeH_8. (g) Each Te was coordinated by 24 H atoms in C_2TeH_8.

and 174.9 meV/atom at 300 GPa, respectively, above the convex hull. Hence, $CSeH_6$ and C_2TeH_8 are likely to be synthesized as metastable compounds [107].

B. Geometric constructs and bonding feature of Fd-3m $CSeH_6$ and Fm-3m C_2TeH_8

Structurally, the hydrogen-rich $CSeH_6$ phase crystallized into a cubic structure with space group Fd-3m [8 f.u. per cell; Fig. 2(a)]. Interestingly, the Se atoms with a Se-Se distance of 2.42 Å at 300 GPa had a consistent stacking pattern with those of C atoms in diamond [Fig. 2(a)]. Each C atom was sixfold coordinated with an H atom to constitute a CH_6 octahedra with equal C-H distances of 1.13 Å at 300 GPa [Fig. 2(b)]. These CH_6 units were evenly distributed in the diamondlike Se framework [Figs. 2(a) and 2(c)]. Meanwhile, each Se atom was surrounded by six H atoms and formed an SeH_6 unit Se-H bond length of 1.67 Å [Fig. 2(d)], which is analogous to SeH_6 in cubic H_3Se [79] and SH_6 in Im-3m-structured H_3S [13]. $CSeH_6$ can be considered as the assembly of octahedral CH_6 and SeH_6 through a vertex-sharing pattern [Fig. 2(b)]. All hydrogen atoms in $CSeH_6$ were separated by C and Se atoms [Figs. 2(a) and 2(b)]. In contrast, C_2TeH_8 had cubic Fm-3m symmetry [2 f.u. per cell; Fig. 2(e)]. The Te atoms featured a face-centered cubic lattice. Notably, unlike the CH_6 unit of $CSeH_6$, each C and four H atoms in C_2TeH_8 formed a CH_4 tetrahedron with a C-H bond length of 1.13 Å at 300 GPa, which was situated exactly at the tetrahedral site of the Te lattice [Fig. 2(e)]. Interestingly, a polyhedron with 26 sides consisted of one Te and 24 coordinated H atoms with a Te-H spacing of 2.08 Å, where the coordination number of Te was larger than 14 in R-3m-structured H_4Te [83], and these polyhedra presented face-sharing stacks [Figs. 2(f) and 2(g)]. More strikingly, the hydrogen atoms formed a cube-shaped building block with a distance of 1.19 Å [Fig. 2(f)], which is slightly larger than 0.98 Å of hydrogen-hydrogen distance in the $I4_1/amd$ structure at 500 GPa [108]. Similar to the H_8 cubes in LaH_{10}, these H_8 cubes were interconnected by CH_4 tetrahedral units and constituted a three-dimensional network, where Te occupied the center of the caged C-H frame and served as an electron donor. The peculiar hydrogen motifs may induce the superconductivity of $CSeH_6$ and C_2TeH_8, which will be discussed later.

To analyze the bonding nature of Fd-3m-structured $CSeH_6$ and Fm-3m-structured C_2TeH_8, the electron localization functions (ELFs) [109] at 300 GPa were calculated. Figure S1 of the Supplemental Material [101] shows pronounced electron localization, as evidenced by large ELF values above 0.5, between Se and H and between C and H, which indicates that a covalent Se-H bond formed in $CSeH_6$ and a C-H covalent bond formed in both $CSeH_6$ and C_2TeH_8. The ELF values between Se-Se bonds in the diamondlike Se lattice of $CSeH_6$

were close to 0.5, i.e., similar to those between H-H bonds in C_2TeH_8, which implies the formation of metallic Se-Se and H-H bonds. Bader charge calculations [110] of $CSeH_6$ and C_2TeH_8 at 300 GPa were implemented to evaluate the interatomic charge transfer. The results show that both Se and H were electron donors, whereas C was the electron acceptor (Table S2 of the Supplemental Material [101]), which also demonstrates the polar covalent C-H and ionic C-Se bonds. In contrast, each Te atom lost 1.668e, while C and H gained 0.77 and 0.016e, respectively, which suggests the Te-C and Te-H ionic bonding (Table S2). To assess the interatomic interactions, we calculated the crystal orbital Hamilton populations (COHPs) as achieved in the LOBSTER package [111,112] of adjacent atomic pairs in $CSeH_6$ and C_2TeH_8 at 300 GPa. Furthermore, a negative COHP value represents a bonding state, while a positive COHP value represents an antibonding state. Figure S2 shows the significant negative COHP of C-H, Se-H, and Se-Se pairs below the Fermi level E_f in $CSeH_6$, which implies that the C-H, Se-H, and Se-Se interactions play a crucial role in structural stability. For C_2TeH_8, the C-H and Te-C pairs had apparently negative COHP below E_f compared to the H-H pair, which suggests the dominant role of the C-H and Te-C interactions in stabilizing the structure. The integrated COHPs (ICOHPs) up to E_f were used to evaluate the bond strength. In Table S3, the ICOHPs of C-H, Se-H, and Se-Se in $CSeH_6$ were −6.937, −2.883, and −1.291 eV/pair, respectively, which shows that C-H bonds are much stronger than Se-H and Se-Se bonds. For C_2TeH_8, C-H, Te-C, Te-H, and H-H pairs had ICOHPs of −6.955, −2.540, −0.179, and −1.098 eV/pair, respectively, which indicates that the C-H interactions are stronger than those of Te-C, Te-H, and H-H.

C. Fd-3m $CSeH_6$ with high-T_c superconductivity

Motivated by the striking structure and high hydrogen content of $CSeH_6$, we examined its electronic structure information. The calculated electronic band structure of $CSeH_6$ at 300 GPa in Fig. 3(a) with obvious dispersion characteristics indicates strong interactions between atoms, which is consistent with the chemical bonding analysis. Interestingly, the flat band appeared near the Fermi level E_f along the Γ-X direction in the Brillouin zone, which is in contrast with other high-symmetry directions, such as the apparent electron pockets in the Γ-L path. Four bands (named bands 1, 2, 3, and 4) straddled the Fermi level and elucidate the emergence of metallization in $CSeH_6$. Meanwhile, the Wannier-interpolated band structure of Fd-3m $CSeH_6$ at 300 GPa was computed by the interpolation with maximally localized Wannier functions in the WANNIER90 code [113]. Figure S3 shows that the Wannier-interpolated band structure of $CSeH_6$ was generally consistent with the density functional theory results near the Fermi level. To reveal the origin of the metallicity of $CSeH_6$, the corresponding projected density of states (PDOS) at 300 GPa was computed [Fig. 3(b)]. Se 4p states dominated at the Fermi energy in comparison with C 2s, C 2p, Se 4s, and H 1s, which played a role in the conductivity of $CSeH_6$. Further analysis shows marked orbital overlapping between C 2p and H 1s below E_f and between Se 4p and H 1s, which demonstrates the strong C-H and Se-H bonds. Similar to H_3Se [79], the obvious

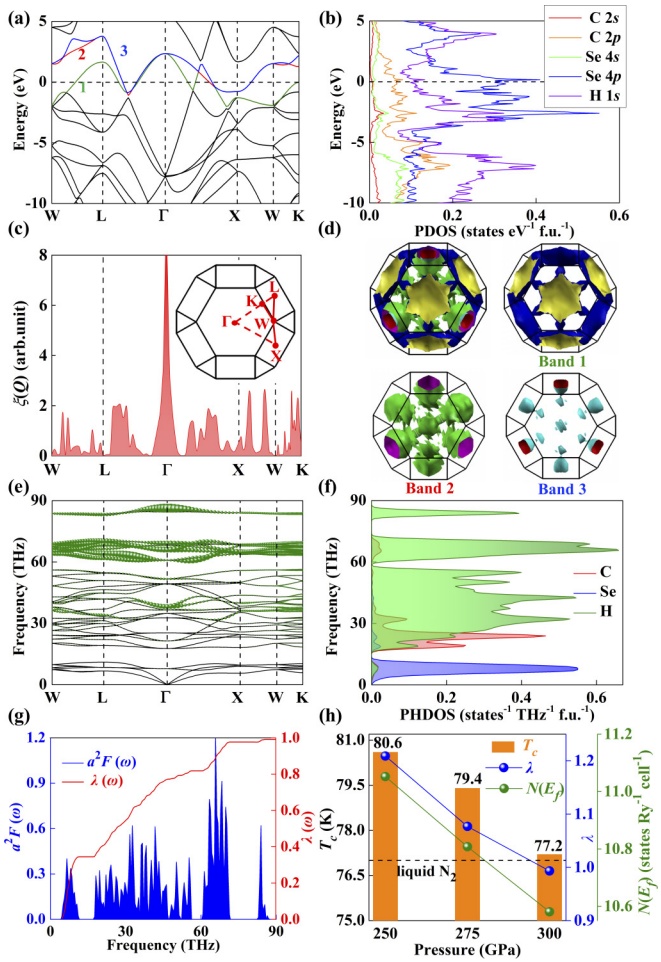

FIG. 3. Electronic and superconductive properties of Fd-3m $CSeH_6$. (a) Electronic band structure of the primitive cell structure of $CSeH_6$ at 300 GPa. The Fermi energy E_f was set to zero. (b) Projected density of states (PDOS) of $CSeH_6$ at 300 GPa. The horizontal dashed line signifies the Fermi level. (c) Fermi-surface nesting function of $CSeH_6$ at 300 GPa. The subplot is the Brillouin zone of $CSeH_6$ in the reciprocal space; the red lines represent the paths of high-symmetry k points. (d) Three-dimensional merged Fermi surface (FS) and decomposed Fermi surfaces of $CSeH_6$ at 300 GPa. (e) Phonon dispersion of the primitive cell structure of $CSeH_6$ at 300 GPa, where the size of the green balls corresponds to the magnitude of the phonon linewidth $\gamma_{q,j}(\omega)$. (f) Phonon density of states (PHDOS) per formula of $CSeH_6$ at 300 GPa. (g) Frequency-dependent Eliashberg spectral function $\alpha^2F(\omega)$ and partial electron-phonon coupling (EPC) parameter $\lambda(\omega)$. (h) Superconducting critical temperature T_c, integrated EPC constant λ, and total electron density of states $N(E_f)$ at E_f of $CSeH_6$ as functions of the pressure, where the vertical coordinate of the horizontal dashed line corresponds to the boiling point of liquid nitrogen.

van Hove singularity contributed by Se 4p formed near E_f, which induced the formation of the above flat band and electron pockets. Meanwhile, the nesting function $\xi(Q)$ along the high-symmetry path of $CSeH_6$ at 300 GPa was computed to show relatively notable Fermi-surface nesting in the directions of L-Γ and Γ-X [Fig. 3(c)]. An exception is the peak of the nesting function at point Γ [Fig. 3(c)], which is consistent with the calculated Fermi surface [Fig. 3(d)].

This electronic structure analysis is beneficial to the superconductivity.

The electronic properties of Fd-3m-structured $CSeH_6$ imply its high potential superconductivity. We implemented the EPC calculations of $CSeH_6$ at 300 GPa and estimated a high T_c of 77.2 K. The corresponding integral EPC parameter λ was mainly determined by the phonon linewidth $\gamma_{q,j}(\omega)$, which is associated with the electron-phonon interaction matrix element. The EPC matrix element can be used to describe the scattering probability amplitude of an electron on the Fermi surface by a phonon with wave vector $\boldsymbol{q}$. The resulting EPC constant λ was 0.99, which is superior to MgB_2 (0.61) [114] and further suggests that $CSeH_6$ exhibits a strong electron-phonon coupling strength. To reveal the superconducting mechanism of $CSeH_6$, we calculated the Eliashberg spectral function $\alpha^2F(\omega)$, phonon spectrum with the phonon linewidth, and phonon density of states (PHDOS) related to C, Se, and H atoms at 300 GPa. The phonon dispersion curves show no imaginary phonon modes across the entire Brillouin zone, which indicates its dynamical stability [Fig. 3(e)]. Furthermore, the phonon modes were divided into three parts as demonstrated in the PHDOS of Fig. 3(f): (i) The low-frequency phonon modes below 15.1 THz were mainly determined by Se atom vibration and constituted 34.8% of the total EPC parameter λ. (ii) The modes at 15.1–25.6 THz occurred due to the mixed vibration of C and Se atoms and constituted 14.3% of the integrated λ. (iii) High-frequency optical phonon modes above 25.6 THz were related to H atomic vibrations and accounted for 50.9% of the EPC strength λ. Meanwhile, several marked peaks were found in the Eliashberg spectral function [Fig. 3(g)]. In particular, the large peaks at 63.9, 66.1, 68.6, 70.2, and 84.1 THz are related to the large phonon linewidth [Fig. 3(g)] and play an important role in electron-phonon interaction. Therefore, the electron-phonon coupling interactions of $CSeH_6$ are mainly ascribed to the strong coupling between conducting electrons from C 2p, Se 4p, and H 1s orbitals near the Fermi energy and H-associated phonons in the high-frequency region.

High-temperature hydride superconductors at high compression have been reportedly preserved at lower pressures, including Fm-3m $LaBeH_8$ (185 K at 20 GPa) [49]. Accordingly, we focused on the superconducting properties of $CSeH_6$ with decompression. When the pressure gradually decreased to 250 GPa, $CSeH_6$ remained dynamically stable (Fig. S4). Similar to Fm-3m Ca_2H [115] and $P6/mmm$ Sc_2P [116], the critical temperature of $CSeH_6$ increased (79.4 K at 275 GPa, 80.6 K at 250 GPa) with a slope of dT_c/dp of −0.048 K/GPa, which was derived from the enhanced electron-phonon coupling strength λ from 1.08 at 275 GPa to 1.21 at 250 GPa [Fig. 3(h) and Table S4]. Meanwhile, the aggregate electron density of states at the Fermi level $N(E_f)$ of $CSeH_6$ increased upon decompression [Fig. 3(h) and Table S4], which implies that more electrons participate in the coupling with phonons and increase the superconducting transition temperature of $CSeH_6$. Therefore, the high-temperature superconductivity of $CSeH_6$ is mainly determined by the electron-phonon coupling strength and total density of states at the Fermi level. The superconductive critical temperature T_c of $CSeH_6$ with spin-orbit coupling (SOC) at 300 GPa was calculated to evaluate the effect of the SOC. In Table S5, T_c of $CSeH_6$ was estimated to be 77.6 K using $\mu^* = 0.1$, which is slightly higher than the case without SOC. Thus, SOC was found to not alter the main conclusion for the superconductivity of $CSeH_6$. Our further simulations on T_c of $CSeH_6$ at 300 GPa were estimated by using direct numerical solutions to Eliashberg equations [117]. The computed T_c was 78.2 K, which is slightly higher than the value of 77.2 K estimated by the Allen-Dynes-modified McMillan equation (Tables S4 and S6).

D. Fm-3m C_2TeH_8 with pronounced superconductivity

We investigated the electronic and superconducting properties of Fm-3m-structured C_2TeH_8 with unusual H_8 units to obtain a higher superconductive critical temperature. The calculated electronic band structure with atomic contribution at 300 GPa demonstrates that C_2TeH_8 exhibited typical metallicity as evidenced by bands 1, 2, 3, and 4 crossing the Fermi level [Figs. 4(a) and S5]. Further analysis shows that bands 1 and 2 near the Fermi energy E_f mainly resulted from Te and H atoms (Figs. S5 and S6). Band 3 at E_f was primarily derived from the C, Te, and H atomic contributions. In comparison, band 4 near E_f was principally contributed by C and Te atoms (Figs. S5 and S6). Meanwhile, the Fermi surfaces (FSs) that corresponded to the energy bands across E_f were calculated. FS1 and FS2 contained maximum Fermi velocities, whereas low and medium Fermi velocities emerge on all four FSs [Figs. 4(d) and S7], which indicates the nesting of Fermi surfaces. The calculated Fermi-surface nesting function also shows marked Fermi-surface nesting along the W-L direction compared to other directions in the Brillouin zone [Figs. 4(d) and S7]. There was significant band dispersion in the entire Brillouin zone, which resulted in a more obvious electron pocket near the Fermi energy at point Γ than that of $CSeH_6$ [Fig. 4(a)]. Considering that C_2TeH_8 has heavy element Te, the band structure with SOC at 300 GPa was calculated. In Fig. 4(c), the SOC hardly affected the electronic band structure of C_2TeH_8. The analysis of the PDOS shows that the excellent conductivity of C_2TeH_8 was mainly induced by C 2p, Te 5p, and H 1s states near the Fermi level, which formed van Hove singularities [Fig. 4(b)]. The Te 5p states had a larger contribution than H 1s, and H 1s states contributed more than C 2p states at E_f, which indicates the dominance of Te atoms [Fig. 4(b)]. The orbital overlaps between C 2p and Te 5p and between C 2p and H 1s below the Fermi energy [Fig. 4(b)] indicate strong interactions between C and Te or between C and H, which further supports the bonding analysis.

The exceptional electronic structure indicates that metallic C_2TeH_8 could be a superconductor. Furthermore, the superconductive properties of Fm-3m-structured C_2TeH_8 under compression were investigated. The phonon spectrum calculations of C_2TeH_8 at 300 GPa were first performed to evaluate its lattice dynamic stability. The results reveal that C_2TeH_8 has robust stability in dynamics and exhibits separated features of acoustic and optical phonon branches [Fig. 4(e)], which is clearly distinct from those of $CSeH_6$. The EPC calculations display that C_2TeH_8 had a remarkably high transition temperature T_c value of 123.4 K at 300 GPa when $\mu^* = 0.10$, which is significantly higher than 77.2 K of $CSeH_6$ at the same pressure, thus elucidating its high-temperature

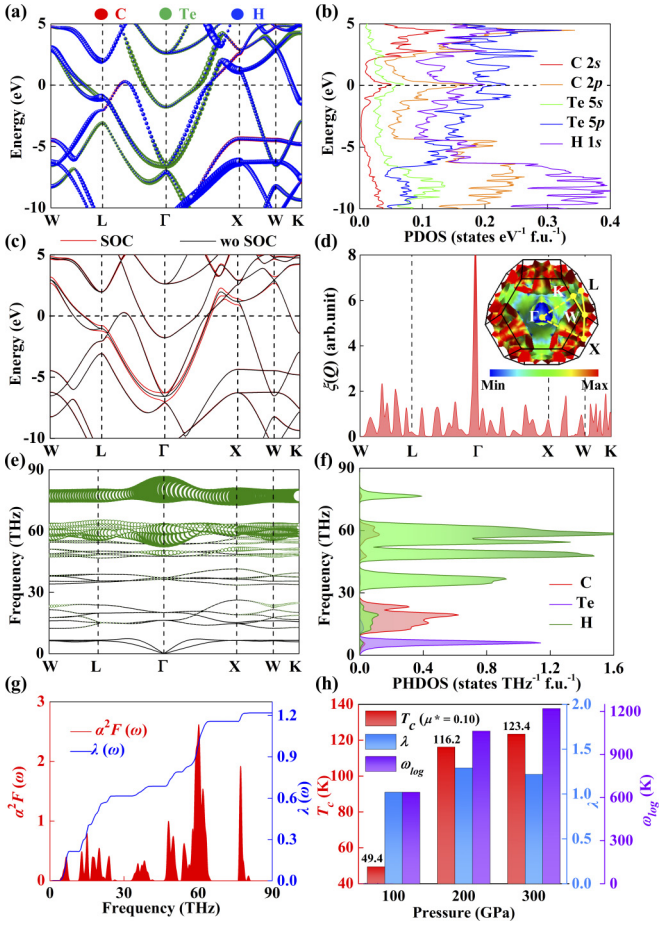

FIG. 4. Electronic structures and superconducting properties of Fm-$3m$ C_2TeH_8. (a) Orbital-resolved electronic band structure of the primitive cell structure of C_2TeH_8 at 300 GPa. The contribution of C, Te, and H atoms per formula is proportional to the size of the circles. (b) Projected density of states (PDOS) per formula of C_2TeH_8 at 300 GPa. (c) Comparison of the electronic band structures of C_2TeH_8 with and without spin-orbital coupling at 300 GPa. (d) Fermi-surface nesting function of C_2TeH_8 at 300 GPa. The subplot is a three-dimensional merged Fermi surface (FS), where the color gradient indicates the magnitude of the Fermi velocity. (e) Phonon spectrum of C_2TeH_8 at 300 GPa. The size of the green circles illustrates the phonon linewidth $\gamma_{q,j}(\omega)$ of each mode (q, j). (f) Frequency-dependent phonon density of states (PHDOS) per formula of C_2TeH_8 at 300 GPa. (g) Eliashberg spectral function $\alpha^2F(\omega)$ and partial electron-phonon coupling parameter $\lambda(\omega)$ of C_2TeH_8 at 300 GPa. (h) Corresponding evolution of the critical temperature T_c, cumulative electron-phonon coupling constant λ, and logarithmic average phonon frequency $\omega_{\log}$ in the pressure range of 100–300 GPa.

superconducting properties. The superconducting mechanism analysis mainly attributed the high-temperature superconductivity of C_2TeH_8 to the large average phonon frequency $\omega_{\log}$ [Fig. 4(h)]. Meanwhile, C_2TeH_8 has an EPC parameter λ of 1.22 at 300 GPa, which is obviously larger than 0.61 of the ambient-pressure superconductor MgB_2 and reveals the sizable EPC strength in C_2TeH_8. Then, we computed T_c of C_2TeH_8 at 300 GPa by solving Eliashberg equations [117]. The resulting superconducting transition temperature of C_2TeH_8 was 151.4 K at 300 GPa (Table S6), which is notably larger than the value of 123.4 K calculated by the Allen-Dynes-modified McMillan equation and indicates that C_2TeH_8 is a strongly coupled superconductor. The electron-phonon coupling analysis shows that the low-frequency acoustic phonon modes below 9.4 THz, which were mainly derived from the Te atom vibration, constituted 17.5% of the cumulative EPC parameter λ [Fig. 4(g)]. In contrast, the phonon modes at 9.4–28.1 THz, which are principally related to the vibrations of C atoms, constituted 33% of the total λ. The H-dominated high-frequency optical phonon modes above 31.7 THz constituted 49.5% of the integral λ [Fig. 4(g)]. Therefore, the strong EPC strength of C_2TeH_8 is mainly ascribed to the coupling between the C- and H-derived optical phonons and the electrons from C $2p$, Te $5p$, and H $1s$ at approximately the Fermi level. The PHDOS analysis shows mixed vibrational modes of C and H atoms in the relatively low- and high-frequency domains [Fig. 4(f)]. The large magnitude of Eliashberg spectral function $\alpha^2F(\omega)$ was at approximately 60.2 and 77.3 THz [Fig. 4(g)], which is associated with the large phonon linewidth and favorably contributes to the electron-phonon interaction [Fig. 4(e)]. In particular, the notable phonon linewidth with the highest-frequency branch at the Γ point in the Brillouin zone resulted from the H atom vibrations (Fig. S8). T_c of C_2TeH_8 at 300 GPa, which included the SOC, was estimated to be 123.9 K for $\mu^* = 0.10$. Since this value is slightly higher than that without considering SOC, the SOC may slightly influence the superconductivity of C_2TeH_8, which is consistent with the electronic band structure analysis.

The pressure-dependent evolution of the superconducting transition temperature of C_2TeH_8 was further explored. With decreasing pressure, C_2TeH_8 remained dynamically stable at 100 GPa (Fig. S9), and its superconductivity was suppressed [Fig. 4(h)], which is analogous to $I4/mmm$ Sc_3P [116] and differs from $CSeH_6$. C_2TeH_8 maintained high-temperature superconductivity despite the pressure-induced decrease in superconducting transition temperature T_c (49.4 K at 100 GPa; 116.2 K at 200 GPa) in comparison to 39 K of MgB_2 at ambient pressure [Fig. 4(h)]. Further analysis demonstrated that the decrease in critical temperatures under decompression predominantly derived from the cooperative interaction between relatively strong electron-phonon coupling strength λ and weakened logarithmic average phonon frequency $\omega_{\log}$ (Table S4), which is different from the superconductive mechanism of $CSeH_6$.

In addition, since Fd-$3m$ $CSeH_6$ and Fm-$3m$ C_2TeH_8 hydrides have outstanding superconductivity, we studied the superconductivity of the Fd-$3m$ $CTeH_6$ and Fm-$3m$ C_2SeH_8 at 300 GPa by replacing Se/Te with Te/Se based on the template hydrides $CSeH_6$ and C_2TeH_8, respectively. Both $CTeH_6$ and C_2SeH_8 are dynamically stable at 300 GPa because there is no negative phonon frequency value across the Brillouin zone (Figs. S10 and S11). High phonon frequencies dominated by hydrogen atoms were uncovered in both $CTeH_6$ and C_2SeH_8, which set the stage for their high-temperature superconductivity (Figs. S10 and S11). Meanwhile, both $CTeH_6$ and C_2SeH_8 exhibited excellent metal characteristics as indicated by several bands crossing the Fermi energy and the apparent electron states from C $2p$, Te $5p$, Se $4p$, and H $1s$ at approximately the Fermi level (Figs. S10 and S11). Further

calculations on the electron-phonon coupling suggest that the superconducting transition temperature of $CTeH_6$ is 61.3 K at 300 GPa ($\mu^* = 0.1$), which is slightly smaller than that of $CSeH_6$ at identical pressure (Tables S4 and S7). This result is mainly attributed to the relatively weak electron-phonon strength λ of 0.77 and low electronic density of states at the Fermi level of $CTeH_6$ (Tables S4 and S7). In contrast, the calculated T_c value at 300 GPa ($\mu^* = 0.1$) for C_2SeH_8 is 80.8 K, which is lower than 151.4 K of C_2TeH_8, mainly because C_2SeH_8 has a relatively small logarithmic average phonon frequency $\omega_{\log}$ of 739.6 K and low electron states near the Fermi energy (Tables S4 and S7).

IV. CONCLUSIONS

In this study, we systematically explored C-Se-H and C-Te-H ternary hydrides with high hydrogen content at high pressure using a state-of-the-art structure search approach with first-principles calculations. Two hitherto unknown cubic $CSeH_6$ and C_2TeH_8 with metastability and metallicity were proposed. Intriguingly, Fd-$3m$ $CSeH_6$ had a diamondlike Se sublattice, where octahedral CH_6 units were located at the corresponding cavity; Fm-$3m$ C_2TeH_8 had striking H_8 cubes that connected with the CH_4 tetrahedron. Furthermore, superconducting properties calculations revealed that $CSeH_6$ had a high critical temperature of 80.6 K at 250 GPa, which exceeded the liquid-nitrogen temperature (77 K). This high critical temperature was chiefly attributed to the coupling of the C $2p$, Se $4p$, and H $1s$ states at approximately Fermi energy with high-frequency H-derived phonons. In contrast, C_2TeH_8 had a higher transition temperature of 151.4 K at 300 GPa due to the large average phonon frequency and the coupling between C- or H-associated phonons and C $2p$, Te $5p$, and H $1s$ electronic states near the Fermi energy. Our current work stimulated future research exploration of high-temperature superconductivity among multinary hydrides.

ACKNOWLEDGMENTS

The authors acknowledge funding support from the National Natural Science Foundation of China under Grants No. 11704062 and No. 12074138, the funding from Education Department of Jilin Province under Grant No. JJKH20221152KJ, the "111" Project (No. B13013), the funding from Jilin Province (No. 20220502002GH), the Foundation of Basic Science (Natural Science) Research Program for Higher Education Institutions in Jiangsu Province (23KJD140003), and the Foundation of Nanjing Xiaozhuang University (Grant No. 2022NXY25).

APPENDIX: TERNARY SUPERCONDUCTING HYDRIDES

In this section, some ternary hydride superconductors at different pressures are shown in Table I, which mainly include metal-free, single metal, and dual metal ternary hydrides.

TABLE I. Some reported ternary superconducting hydrides.

Categories	Ternary hydrides	Pressure (GPa)	T_c (K)
Metal-free hydrides	H_6SSe	200	196–115 [118]
	H_6SF	25	121 [119]
	H_6SCl	90	155.4 [120]
	H_6SBr	140	136.4 [120]
Single metal hydrides	YSH_6	210	91 [121]
	LiP_2H_{14}	230	169 [122]
	$LiSiH_8$	250	77 [123]
	$SrSiH_8$	27	126 [124]
	AlC_2H_8	80	67 [125]
	YCH_{12}	180	112 [126]
	$NaBH_3$	300	86.8 [127]
	KB_2H_8	12	134–146 [128]
	Rb/CsB_2H_8	25	∼100 [129]
	$CaBH_7$	200	200 [130]
	$LaBH_8$	50–55	126–156 [131,132]
	$LaH_{9.985}N_{0.015}$	240	288 [133]
Dual metal hydrides	K_2ReH_9	75	127.1 [134]
	$CaYH_{12}$	200	258 [135]
	Li_2ScH_{20}	300	242 [136]
	Li_2NaH_{17}	300	340 [137]
	$LiNa_3H_{23}$	350	310 [137]
	YLu_3H_{24}	110	288 [138]
	Y_3CaH_{24}	150	242–258 [139]
	$LaYH_{12}$	200	140 [140]
	$(Y, Sr)H_{11}$	175	240 [141]
	$(La, Y)H_4$	110	92 [142]
	$(La, Y)H_{10}$	183	253 [143]
	$(La, Ce)H_9$	172	178 [144]
	$Y_{0.5}Ce_{0.5}H_9$	98–200	97–141 [145]
	La_3ThH_{40}	200	242 [146]
	$AcBeH_8$	10	181 [147]

[1] W. E. Pickett, *Colloquium*: Room temperature superconductivity: The roles of theory and materials design, Rev. Mod. Phys. **95**, 021001 (2023).

[2] J. A. Flores-Livas, L. Boeri, A. Sanna, G. Profeta, R. Arita, and M. Eremets, A perspective on conventional high-temperature superconductors at high pressure: Methods and materials, Phys. Rep. **856**, 1 (2020).

[3] X. Zhou, W. S. Lee, M. Imada, N. Trivedi, P. Phillips, H. Y. Kee, P. Törmä, and M. Eremets, High-temperature superconductivity, Nat. Rev. Phys. **3**, 462 (2021).

[4] B. Lilia *et al.*, The 2021 room-temperature superconductivity roadmap, J. Phys.: Condens. Matter **34**, 183002 (2022).

[5] H. Tran and T. N. Vu, Machine-learning approach for discovery of conventional superconductors, Phys. Rev. Mater. **7**, 054805 (2023).

[6] C. J. Pickard, I. Errea, and M. I. Eremets, Superconducting hydrides under pressure, Annu. Rev. Condens. Matter Phys. **11**, 57 (2020).

[7] D. Duan, Y. Liu, Y. Ma, Z. Shao, B. Liu, and T. Cui, Structure and superconductivity of hydrides at high pressures, Natl. Sci. Rev. **4**, 121 (2017).

[8] V. S. Minkov, V. Ksenofontov, S. L. Bud'ko, E. F. Talantsev, and M. I. Eremets, Magnetic flux trapping in hydrogen-rich high-temperature superconductors, Nat. Phys. **19**, 1293 (2023).

[9] F. Belli, T. Novoa, J. Contreras-García, and I. Errea, Strong correlation between electronic bonding network and critical temperature in hydrogen-based superconductors, Nat. Commun. **12**, 5381 (2021).

[10] G. Gao, L. Wang, M. Li, J. Zhang, R. T. Howie, E. Gregoryanz, V. V. Struzhkin, L. Wang, and J. S. Tse, Superconducting binary hydrides: Theoretical predictions and experimental progresses, Mater. Today Phys. **21**, 100546 (2021).

[11] H. Wang, X. Li, G. Gao, Y. Li, and Y. Ma, Hydrogen-rich superconductors at high pressures, Wiley Interdiscip. Rev. Comput. Mol. Sci. **8**, e1330 (2018).

[12] A. Shamp and E. Zurek, Superconductivity in hydrides doped with main group elements under pressure, Novel Superconduct. Mater. **3**, 14 (2017).

[13] D. Duan, Y. Liu, F. Tian, D. Li, X. Huang, Z. Zhao, H. Yu, B. Liu, W. Tian, and T. Cui, Pressure-induced metallization of dense $(H_2S)_2H_2$ with high-T_c superconductivity, Sci. Rep. **4**, 6968 (2014).

[14] I. Errea, M. Calandra, C. J. Pickard, J. Nelson, R. J. Needs, Y. Li, H. Liu, Y. Zhang, Y. Ma, and F. Mauri, High-pressure hydrogen sulfide from first principles: A strongly anharmonic phonon-mediated superconductor, Phys. Rev. Lett. **114**, 157004 (2015).

[15] A. P. Drozdov, M. I. Eremets, I. A. Troyan, V. Ksenofontov, and S. I. Shylin, Conventional superconductivity at 203 kelvin at high pressures in the sulfur hydride system, Nature (London) **525**, 73 (2015).

[16] H. Wang, J. S. Tse, K. Tanaka, T. Iitaka, and Y. Ma, Superconductive sodalite-like clathrate calcium hydride at high pressures, Proc. Natl. Acad. Sci. USA **109**, 6463 (2012).

[17] F. Peng, Y. Sun, C. J. Pickard, R. J. Needs, Q. Wu, and Y. Ma, Hydrogen clathrate structures in rare earth hydrides at high pressures: Possible route to room-temperature superconductivity, Phys. Rev. Lett. **119**, 107001 (2017).

[18] H. Liu, I. I. Naumov, R. Hoffmann, N. W. Ashcroft, and R. J. Hemley, Potential high-T_c superconducting lanthanum and yttrium hydrides at high pressure, Proc. Natl. Acad. Sci. USA **114**, 6990 (2017).

[19] Y. Sun, X. Zhong, H. Liu, and Y. Ma, Clathrate metal superhydrides at high-pressure conditions: Enroute to room-temperature superconductivity, Natl. Sci. Rev., nwad270 (2023).

[20] L. Ma *et al.*, High-temperature superconducting phase in clathrate calcium hydride CaH_6 up to 215 K at a pressure of 172 GPa, Phys. Rev. Lett. **128**, 167001 (2022).

[21] Z. Li *et al.*, Superconductivity above 200 K discovered in superhydrides of calcium, Nat. Commun. **13**, 2863 (2022).

[22] A. P. Drozdov *et al.*, Superconductivity at 250 K in lanthanum hydride under high pressures, Nature (London) **569**, 528 (2019).

[23] M. Somayazulu, M. Ahart, A. K. Mishra, Z. M. Geballe, M. Baldini, Y. Meng, V. V. Struzhkin, and R. J. Hemley, Evidence for superconductivity above 260 K in lanthanum superhydride at megabar pressures, Phys. Rev. Lett. **122**, 027001 (2019).

[24] X. Zhang, Y. Zhao, and G. Yang, Superconducting ternary hydrides under high pressure, WIREs Comput. Mol. Sci. **12**, e1582 (2022).

[25] Y. Sun, S. Sun, X. Zhong, and H. Liu, Prediction for high superconducting ternary hydrides below megabar pressure, J. Phys.: Condens. Matter **34**, 505404 (2022).

[26] D. Hou, D. Meng, J. Kang, Z. Zhang, C. Zhao, R. Sun, D. She, and W. Yue, Superconductivity in ternary hydrides at high pressure, Mod. Phys. Lett. B **36**, 2230002 (2022).

[27] P. Shan, L. Ma, and J. Cheng, Ternary superhydrides for high-temperature superconductivity at low pressures, Natl. Sci. Rev. nwae003 (2024).

[28] W. Zhao, X. Huang, Z. Zhang, S. Chen, M. Du, D. Duan, and T. Cui, Superconducting ternary hydrides: Progress and challenges, Natl. Sci. Rev. nwad307 (2023).

[29] D. Li, Y. Liu, F.-B. Tian, S.-L. Wei, Z. Liu, D.-F. Duan, B.-B. Liu, and T. Cui, Pressure-induced superconducting ternary hydride H_3SXe: A theoretical investigation, Front. Phys. **13**, 137107 (2018).

[30] L.-T. Shi, R. Turnbull, A. Liang, X.-R. Chen, and G.-F. Ji, Metallization and superconductivity of NBH_{12} compounds stabilized by dihydrogen bonds, J. Mater. Chem. C **10**, 3081 (2022).

[31] N. Geng, T. Bi, and E. Zurek, Structural diversity and superconductivity in S–P–H ternary hydrides under pressure, J. Phys. Chem. C **126**, 7208 (2022).

[32] Y. Zhao, X. Zhang, Y. Liu, and G. Yang, Theoretical considerations of superconducting $HfBH_2$ and HfB_2H under high pressure, J. Appl. Phys. **130**, 153904 (2021).

[33] S. Wu, B. Li, Z. Chen, Y. Hou, Y. Bai, X. Hao, Y. Yang, S. Liu, J. Cheng, and Z. Shi, Phase transitions and superconductivity in ternary hydride Li_2SiH_6 at high pressures, J. Appl. Phys. **131**, 65901 (2022).

[34] X. Li, X. Zhang, A. Bergara, G. Gao, Y. Liu, and G. Yang, Superconducting LaP_2H_2 with graphenelike phosphorus layers, Phys. Rev. B **105**, 024504 (2022).

[35] M. Gao, P.-J. Guo, H.-C. Yang, X.-W. Yan, F. Ma, Z.-Y. Lu, T. Xiang, and H.-Q. Lin, Stabilizing a hydrogen-rich superconductor at 1 GPa by charge transfer modulated virtual high-pressure effect, Phys. Rev. B **107**, L180501 (2023).

[36] Z. Shao, D. Duan, Y. Ma, H. Yu, H. Song, H. Xie, D. Li, F. Tian, B. Liu, and T. Cui, Ternary superconducting cophosphorus hydrides stabilized via lithium, npj Comput. Mater. **5**, 104 (2019).

[37] M.-J. Jiang, H.-L. Tian, Y.-L. Hai, N. Lu, P.-F. Tong, S.-Y. Wu, W.-J. Li, C.-L. Yang, and G.-H. Zhong, Phonon-mediated low-pressure superconductivity in ternary hydride Ba–CH_4, ACS Appl. Electron. Mater. **3**, 4172 (2021).

[38] P. P. Ferreira, L. J. Conway, A. Cucciari, S. Di Cataldo, F. Giannessi, E. Kogler, L. T. F. Eleno, C. J. Pickard, C. Heil, and L. Boeri, Search for ambient superconductivity in the Lu-N-H system, Nat. Commun. **14**, 5367 (2023).

[39] K. Zhang, W. Chen, Y. Zhang, J. Guo, S. Chen, X. Huang, and T. Cui, High-pressure synthesis of a ternary yttrium-sulfur hydride superconductor with a high T_c of approximately 235 K, Sci. China: Phys., Mech. Astron. **67**, 238211 (2024).

[40] D. Meng, M. Sakata, K. Shimizu, Y. Iijima, H. Saitoh, T. Sato, S. Takagi, and S. Orimo, Superconductivity of the

hydrogen-rich metal hydride Li_5MoH_{11} under high pressure, Phys. Rev. B **99**, 024508 (2019).

[41] M. Rahm, R. Hoffmann, and N. W. Ashcroft, Ternary gold hydrides: Routes to stable and potentially superconducting compounds, J. Am. Chem. Soc. **139**, 8740 (2017).

[42] H. Song, Z. Zhang, M. Du, Q. Jiang, D. Duan, and T. Cui, Phase diagrams and superconductivity of ternary Na-Al-H compounds at high pressure, Phys. Rev. B **104**, 104509 (2021).

[43] Y. Ma, D. Duan, Z. Shao, D. Li, L. Wang, H. Yu, F. Tian, H. Xie, B. Liu, and T. Cui, Prediction of superconducting ternary hydride $MgGeH_6$: From divergent high-pressure formation routes, Phys. Chem. Chem. Phys. **19**, 27406 (2017).

[44] W. Chen, X. Huang, D. V. Semenok, S. Chen, D. Zhou, K. Zhang, A. R. Oganov, and T. Cui, Enhancement of superconducting properties in the La–Ce–H system at moderate pressures, Nat. Commun. **14**, 2660 (2023).

[45] X. Dou, X. Kuang, W. Sun, G. Jiang, C. Lu, and A. Hermann, Ternary Mg-Nb-H polyhydrides under high pressure, Phys. Rev. B **104**, 224510 (2021).

[46] P. Song, Z. Hou, K. Nakano, K. Hongo, and R. Maezono, Potential high-T_c superconductivity in $YCeH_x$ and $LaCeH_x$ under pressure, Mater. Today Phys. **28**, 100873 (2022).

[47] Z. Wan, T. Yang, W. Xu, and R. Zhang, Superconductivity and magnetism in compressed actinium-beryllium-hydrogen alloys, arXiv:2209.01903.

[48] L.-T. Shi, J.-G. Si, R. Turnbull, A. Liang, P.-F. Liu, and B.-T. Wang, Prediction of pressure-induced superconductivity in the ternary systems $YScH_{2n}$ (n = 3-6), Phys. Rev. B **109**, 054512 (2024).

[49] Z. Zhang, T. Cui, M. J. Hutcheon, A. M. Shipley, H. Song, M. Du, V. Z. Kresin, D. Duan, C. J. Pickard, and Y. Yao, Design principles for high-temperature superconductors with a hydrogen-based alloy backbone at moderate pressure, Phys. Rev. Lett. **128**, 047001 (2022).

[50] Y. Song, J. Bi, Y. Nakamoto, K. Shimizu, B. Zou, H. Wang, G. Liu, and Y. Ma, Stoichiometric ternary superhydride $LaBeH_8$ as a new template for high-temperature superconductivity at 110 K under 80 GPa, Phys. Rev. Lett. **130**, 266001 (2023).

[51] D. Zhou, D. V. Semenok, D. Duan, H. Xie, W. Chen, X. Huang, X. Li, B. Liu, A. R. Oganov, and T. Cui, Superconducting praseodymium superhydrides, Sci. Adv. **6**, eaax6849 (2023).

[52] A. Shamp, T. Terpstra, T. Bi, Z. Falls, P. Avery, and E. Zurek, Decomposition products of phosphine under pressure: PH_2 stable and superconducting? J. Am. Chem. Soc. **138**, 1884 (2016).

[53] Y. Yuan, Y. Li, G. Fang, G. Liu, C. Pei, X. Li, H. Zheng, K. Yang, and L. Wang, Stoichiometric evolutions of PH_3 under high pressure: Implication for high-T_c superconducting hydrides, Natl. Sci. Rev. **6**, 524 (2019).

[54] D. Zhou *et al.*, High-pressure synthesis of magnetic neodymium polyhydrides, J. Am. Chem. Soc. **142**, 2803 (2020).

[55] Y. Yan, T. Bi, N. Geng, X. Wang, and E. Zurek, A metastable $CaSH_3$ phase composed of HS honeycomb sheets that is superconducting under pressure, J. Phys. Chem. Lett. **11**, 9629 (2020).

[56] S. Yao, Q. Song, W. Hu, D. Wang, L. Peng, T. Shi, J. Chen, X. Liu, J. Lin, and X. Chen, Fermi surface topology and anisotropic superconducting gap in electron-doped hydride compounds at high pressure, Phys. Rev. Mater. **6**, 034801 (2022).

[57] K. Yang, W. Cui, J. Hao, J. Shi, and Y. Li, Superconductivity of graphenelike hydrogen in H_2He at high pressure, Phys. Rev. B **107**, 024501 (2023).

[58] W. Sun, B. Chen, X. Li, F. Peng, A. Hermann, and C. Lu, Ternary Na-P-H superconductor under high pressure, Phys. Rev. B **107**, 214511 (2023).

[59] A. Sanna, T. F. T. Cerqueira, Y.-W. Fang, I. Errea, A. Ludwig, and M. A. L. Marques, Prediction of ambient pressure conventional superconductivity above 80 K in hydride compounds, npj Comput. Mater. **10**, 44 (2024).

[60] J. A. Flores-Livas, M. Amsler, C. Heil, A. Sanna, L. Boeri, G. Profeta, C. Wolverton, S. Goedecker, and E. K. U. Gross, Superconductivity in metastable phases of phosphorus-hydride compounds under high pressure, Phys. Rev. B **93**, 020508(R) (2016).

[61] Y. Sun, J. Lv, Y. Xie, H. Liu, and Y. Ma, Route to a superconducting phase above room temperature in electron-doped hydride compounds under high pressure, Phys. Rev. Lett. **123**, 097001 (2019).

[62] H. Xie *et al.*, Hydrogen pentagraphenelike structure stabilized by hafnium: A high-temperature conventional superconductor, Phys. Rev. Lett. **125**, 217001 (2020).

[63] S. Chen, Y. Qian, X. Huang, W. Chen, J. Guo, K. Zhang, J. Zhang, H. Yuan, and T. Cui, High-temperature superconductivity up to 223 K in the Al stabilized metastable hexagonal lanthanum superhydride, Natl. Sci. Rev. **11**, nwad107 (2023).

[64] K. Dolui, L. J. Conway, C. Heil, T. A. Strobel, R. P. Prasankumar, and C. J. Pickard, Feasible route to high-temperature ambient-pressure hydride superconductivity, Phys. Rev. Lett. **132**, 166001 (2024).

[65] A. Lamichhane *et al.*, X-ray diffraction and equation of state of the C–S–H room-temperature superconductor, J. Chem. Phys. **155**, 114703 (2021).

[66] D. R. Harshman and A. T. Fiory, The superconducting transition temperatures of C–S–H based on inter-sublattice S−H4-tetrahedron electronic interactions, J. Appl. Phys. **131**, 15105 (2022).

[67] I. A. Wrona, M. Kostrzewa, K. A. Krok, A. P. Durajski, and R. Szczęśniak, Carbonaceous sulfur hydride system: The strong-coupled room-temperature superconductor with a low value of Ginzburg–Landau parameter, J. Appl. Phys. **131**, 113901 (2022).

[68] Y. Sakai, J. R. Chelikowsky, and M. L. Cohen, Role of carbon in modifying the properties of superconducting hydrogen sulfide, Phys. Rev. Mater. **6**, 044801 (2022).

[69] X. Wang, T. Bi, K. P. Hilleke, A. Lamichhane, R. J. Hemley, and E. Zurek, Dilute carbon in H_3S under pressure, npj Comput. Mater. **8**, 87 (2022).

[70] Z.-W. Liao, Z. Zhang, J.-Y. You, B. Gu, and G. Su, Enhanced superconductivity in C-S-H compounds at high pressure, Phys. Rev. B **105**, L020510 (2022).

[71] M. Gubler, J. A. Flores-Livas, A. Kozhevnikov, and S. Goedecker, Missing theoretical evidence for conventional room-temperature superconductivity in low-enthalpy structures of carbonaceous sulfur hydrides, Phys. Rev. Mater. **6**, 014801 (2022).

[72] Y. Sun, X. Li, T. Iitaka, H. Liu, and Y. Xie, Crystal structures and superconductivity of carbonaceous sulfur hydrides

at pressures up to 300 GPa, Phys. Rev. B **105**, 134501 (2022).

[73] J. B. Mann, T. L. Meek, and L. C. Allen, Configuration energies of the main group elements, J. Am. Chem. Soc. **122**, 2780 (2000).

[74] J. B. Mann, T. L. Meek, E. T. Knight, J. F. Capitani, and L. C. Allen, Configuration energies of the D-block elements, J. Am. Chem. Soc. **122**, 5132 (2000).

[75] M. Rahm, R. Cammi, N. W. Ashcroft, and R. Hoffmann, Squeezing all elements in the periodic table: Electron configuration and electronegativity of the atoms under compression, J. Am. Chem. Soc. **141**, 10253 (2019).

[76] M. Rahm, T. Zeng, and R. Hoffmann, Electronegativity seen as the ground-state average valence electron binding energy, J. Am. Chem. Soc. **141**, 342 (2019).

[77] C. Tantardini and A. R. Oganov, Thermochemical electronegativities of the elements, Nat. Commun. **12**, 2087 (2021).

[78] X. Dong, A. R. Oganov, H. Cui, X.-F. Zhou, and H.-T. Wang, Electronegativity and chemical hardness of elements under pressure, Proc. Natl. Acad. Sci. USA **119**, e2117416119 (2022).

[79] S. Zhang, Y. Wang, J. Zhang, H. Liu, X. Zhong, H.-F. Song, G. Yang, L. Zhang, and Y. Ma, Phase diagram and high-temperature superconductivity of compressed selenium hydrides, Sci. Rep. **5**, 15433 (2015).

[80] J. A. Flores-Livas, A. Sanna, and E. K. U. Gross, High temperature superconductivity in sulfur and selenium hydrides at high pressure, Eur. Phys. J. B **89**, 63 (2016).

[81] E. A. Drzazga-Szcze¸śniak and A. Z. Kaczmarek, Strong-coupling character of superconducting phase in compressed selenium hydride, Mod. Phys. Lett. B **35**, 2150045 (2020).

[82] J. Wu, L.-Z. Zhao, H.-L. Chen, D. Wang, J.-Y. Chen, X. Guo, Q.-J. Zang, and W.-C. Lu, Structures and superconducting properties of ultra-hydrogen-rich selenium hydride H_6Se, Physica Status Solidi **255**, 1800224 (2018).

[83] X. Zhong, H. Wang, J. Zhang, H. Liu, S. Zhang, H.-F. Song, G. Yang, L. Zhang, and Y. Ma, Tellurium hydrides at high pressures: High-temperature superconductors, Phys. Rev. Lett. **116**, 057002 (2016).

[84] Y. Wang, J. Lv, L. Zhu, and Y. Ma, Crystal structure prediction via particle-swarm optimization, Phys. Rev. B **82**, 094116 (2010).

[85] Y. Wang, J. Lv, L. Zhu, and Y. Ma, CALYPSO: A method for crystal structure prediction, Comput. Phys. Commun. **183**, 2063 (2012).

[86] S. Zhang, Q. Yang, X. Zhang, K. Zhao, H. Yu, L. Zhu, and H. Liu, Crystal structures and superconductivity of lithium and fluorine implanted gold hydrides under high pressures, Phys. Chem. Chem. Phys. **23**, 21544 (2021).

[87] H. Zhai, R. Xu, J. Dai, X. Ma, X. Yu, Q. Li, and Y. Ma, Stabilized nitrogen framework anions in the Ga–N system, J. Am. Chem. Soc. **144**, 21640 (2022).

[88] L. Zhang, Y. Wang, J. Lv, and Y. Ma, Materials discovery at high pressures, Nat. Rev. Mater. **2**, 17005 (2017).

[89] X. Wang, Z. Wang, P. Gao, C. Zhang, J. Lv, H. Wang, H. Liu, Y. Wang, and Y. Ma, Data-driven prediction of complex crystal structures of dense lithium, Nat. Commun. **14**, 2924 (2023).

[90] J. Zhang, H. Liu, Y. Ma, and C. Chen, Direct H-He chemical association in superionic FeO_2H_2He at deep-earth conditions, Natl. Sci. Rev. **9**, nwab168 (2022).

[91] G. Kresse and J. Furthmüller, Efficient iterative schemes for *ab initio* total-energy calculations using a plane-wave basis set, Phys. Rev. B **54**, 11169 (1996).

[92] P. E. Blöchl, Projector augmented-wave method, Phys. Rev. B **50**, 17953 (1994).

[93] H. Liu, I. I. Naumov, and R. J. Hemley, Dense hydrocarbon structures at megabar pressures, J. Phys. Chem. Lett. **7**, 4218 (2016).

[94] J. P. Perdew, K. Burke, and M. Ernzerhof, Generalized gradient approximation made simple, Phys. Rev. Lett. **77**, 3865 (1996).

[95] J. P. Perdew, J. A. Chevary, S. H. Vosko, K. A. Jackson, M. R. Pederson, D. J. Singh, and C. Fiolhais, Atoms, molecules, solids, and surfaces: Applications of the generalized gradient approximation for exchange and correlation, Phys. Rev. B **46**, 6671 (1992).

[96] H. J. Monkhorst and J. D. Pack, Special points for Brillouin-zone integrations, Phys. Rev. B **13**, 5188 (1976).

[97] A. Togo, F. Oba, and I. Tanaka, First-principles calculations of the ferroelastic transition between rutile-type and $CaCl_2$-type SiO_2 at high pressures, Phys. Rev. B **78**, 134106 (2008).

[98] P. Giannozzi, S. Baroni, N. Bonini, M. Calandra, R. Car, C. Cavazzoni, D. Ceresoli, G. L. Chiarotti, M. Cococcioni, and I. Dabo, QUANTUM ESPRESSO: A modular and open-source software project for quantum simulations of materials, J. Phys.: Condens. Matter **21**, 395502 (2009).

[99] W. L. McMillan, Transition temperature of strong-coupled superconductors, Phys. Rev. **167**, 331 (1968).

[100] P. B. Allen and R. C. Dynes, Transition temperature of strong-coupled superconductors reanalyzed, Phys. Rev. B **12**, 905 (1975).

[101] See Supplemental Material at http://link.aps.org/supplemental/10.1103/PhysRevB.109.174507 for computational details, structural information, Bader charge analysis integrated crystal orbital Hamilton populations (ICOHPs), and superconductive properties of Fd-3m and Fm-3m at selected pressures; phonon spectra, phonon density of states, electronic structures, and superconducting properties of Fd-3m and Fm-3m at considered pressures.

[102] J. P. Perdew, J. A. Chevary, S. H. Vosko, K. A. Jackson, M. R. Pederson, D. J. Singh, and C. Fiolhais, Erratum: Atoms, molecules, solids, and surfaces: Applications of the generalized gradient approximation for exchange and correlation, Phys. Rev. B **48**, 4978(E) (1993).

[103] K. Parlinski, Z. Q. Li, and Y. Kawazoe, First-principles determination of the soft mode in cubic ZrO_2, Phys. Rev. Lett. **78**, 4063 (1997).

[104] C. Ji *et al.*, Nitrogen in black phosphorus structure, Sci. Adv. **6**, 9206 (2020).

[105] D. Laniel, B. Winkler, T. Fedotenko, A. Pakhomova, S. Chariton, V. Milman, V. Prakapenka, L. Dubrovinsky, and N. Dubrovinskaia, High-pressure polymeric nitrogen allotrope with the black phosphorus structure, Phys. Rev. Lett. **124**, 216001 (2020).

[106] F. P. Bundy, H. T. Hall, H. M. Strong, and R. H. Wentorfjun, Man-made diamonds, Nature (London) **176**, 51 (1955).

[107] W. Sun *et al.*, A map of the inorganic ternary metal nitrides, Nat. Mater. **18**, 732 (2019).

[108] J. M. McMahon and D. M. Ceperley, Ground-state structures of atomic metallic hydrogen, Phys. Rev. Lett. **106**, 165302 (2011).

[109] A. D. Becke and K. E. Edgecombe, A simple measure of electron localization in atomic and molecular systems, J. Chem. Phys. **92**, 5397 (1990).

[110] R. F. W. Bader, Atoms in molecules, Acc. Chem. Res. **18**, 9 (1985).

[111] R. Dronskowski and P. E. Bloechl, Crystal orbital Hamilton populations (COHP): Energy-resolved visualization of chemical bonding in solids based on density-functional calculations, J. Phys. Chem. **97**, 8617 (1993).

[112] S. Maintz, V. L. Deringer, A. L. Tchougréeff, and R. Dronskowski, LOBSTER: A tool to extract chemical bonding from plane-wave based DFT, J. Comput. Chem. **37**, 1030 (2016).

[113] A. A. Mostofi, J. R. Yates, Y.-S. Lee, I. Souza, D. Vanderbilt, and N. Marzari, wannier90: A tool for obtaining maximally-localised Wannier functions, Comput. Phys. Commun. **178**, 685 (2008).

[114] H. J. Choi, D. Roundy, H. Sun, M. L. Cohen, and S. G. Louie, First-principles calculation of the superconducting transition in MgB_2 within the anisotropic Eliashberg formalism, Phys. Rev. B **66**, 020513(R) (2002).

[115] Q. Wang, S. Zhang, H. Li, H. Wang, G. Liu, J. Ma, H. Xu, H. Liu, and Y. Ma, Coexistence of superconductivity and electride states in Ca_2H with an antifluorite-type motif under compression, J. Mater. Chem. A **11**, 21345 (2023).

[116] K. Zhao, Q. Wang, H. Li, B. Gao, S. Wei, L. Zhu, H. Xu, H. Liu, and S. Zhang, Superconductivity in dense scandium-based phosphides, Phys. Rev. B **108**, 174513 (2023).

[117] G. M. Eliashberg, Interactions between electrons and lattice vibrations in a superconductor, Sov. Phys. JETP **11**, 696 (1960).

[118] B. Liu *et al.*, Effect of covalent bonding on the superconducting critical temperature of the H-S-Se system, Phys. Rev. B **98**, 174101 (2018).

[119] Z. Huo, D. Duan, Q. Jiang, Z. Zhang, and T. Cui, Cubic H_3S stabilized by halogens: High-temperature superconductors at mild pressure, Sci. China: Phys. Mech. Astron. **66**, 118211 (2023).

[120] Y.-L. Hai, H.-L. Tian, M.-J. Jiang, H.-B. Ding, Y.-J. Feng, G.-H. Zhong, C.-L. Yang, X.-J. Chen, and H.-Q. Lin, Prediction of high-T_c superconductivity in $H_6SX(X = \mathrm{Cl, Br})$ at pressures below one megabar, Phys. Rev. B **105**, L180508 (2022).

[121] X. Liang *et al.*, First-principles study of crystal structures and superconductivity of ternary YSH_6 and $LaSH_6$ at high pressures, Phys. Rev. B **100**, 184502 (2019).

[122] X. Li, Y. Xie, Y. Sun, P. Huang, H. Liu, C. Chen, and Y. Ma, Chemically tuning stability and superconductivity of P–H compounds, J. Phys. Chem. Lett. **11**, 935 (2020).

[123] P. Zhang, Y. Sun, X. Li, J. Lv, and H. Liu, Structure and superconductivity in compressed Li-Si-H compounds: Density functional theory calculations, Phys. Rev. B **102**, 184103 (2020).

[124] R. Lucrezi, S. Di Cataldo, W. von der Linden, L. Boeri, and C. Heil, In-silico synthesis of lowest-pressure high-T_c ternary superhydrides, npj Comput. Mater. **8**, 119 (2022).

[125] M.-J. Jiang, Y.-L. Hai, H.-L. Tian, H.-B. Ding, Y.-J. Feng, C.-L. Yang, X.-J. Chen, and G.-H. Zhong, High-temperature superconductivity below 100 GPa in ternary C-based hydride MC_2H_8 with molecular crystal characteristics (M = Na, K, Mg, Al, and Ga), Phys. Rev. B **105**, 104511 (2022).

[126] G. Fei, X. Chen, Y. Liu, and X. Liu, Prediction of ternary superconducting YCH_{12} using a novel solid hydrogen source under high pressure, J. Mater. Chem. C **10**, 17594 (2022).

[127] X. Li, X. Zhang, A. Bergara, Y. Liu, and G. Yang, Structural and electronic properties of Na-B-H compounds at high pressure, Phys. Rev. B **106**, 174104 (2022).

[128] M. Gao, X.-W. Yan, Z.-Y. Lu, and T. Xiang, Phonon-mediated high-temperature superconductivity in the ternary borohydride KB_2H_8 under pressure near 12 GPa, Phys. Rev. B **104**, L100504 (2021).

[129] S. Li, H. Wang, W. Sun, C. Lu, and F. Peng, Superconductivity in compressed ternary alkaline boron hydrides, Phys. Rev. B **105**, 224107 (2022).

[130] W.-H. Yang, W.-C. Lu, W. Qin, H.-J. Sun, X.-Y. Xue, K. M. Ho, and C. Z. Wang, Pressure-induced superconductivity in the hydrogen-rich pseudobinary CaB-H_n compounds, Phys. Rev. B **104**, 174106 (2021).

[131] S. Di Cataldo, C. Heil, W. von der Linden, and L. Boeri, $LaBH_8$: Towards high-T_c low-pressure superconductivity in ternary superhydrides, Phys. Rev. B **104**, L020511 (2021).

[132] X. Liang *et al.*, Prediction of high-T_c superconductivity in ternary lanthanum borohydrides, Phys. Rev. B **104**, 134501 (2021).

[133] Y. Ge, F. Zhang, and R. J. Hemley, Room-temperature superconductivity in boron- and nitrogen-doped lanthanum superhydride, Phys. Rev. B **104**, 214505 (2021).

[134] Y. Zhao, X. Zhang, X. Li, S. Ding, Y. Liu, and G. Yang, Emergent superconductivity in K_2ReH_9 under pressure, J. Mater. Chem. C **10**, 14626 (2022).

[135] X. Liang, A. Bergara, L. Wang, B. Wen, Z. Zhao, X.-F. Zhou, J. He, G. Gao, and Y. Tian, Potential high-T_c superconductivity in $CaYH_{12}$ under pressure, Phys. Rev. B **99**, 100505(R) (2019).

[136] Y. Sun, Y. Wang, X. Zhong, Y. Xie, and H. Liu, High-temperature superconducting ternary Li-R-H superhydrides at high pressures (R = Sc, Y, La), Phys. Rev. B **106**, 024519 (2022).

[137] D. An, D. Duan, Z. Zhang, Q. Jiang, H. Song, and T. Cui, Thermodynamically stable room-temperature superconductors in Li-Na hydrides under high pressures, arXiv:2303.09805.

[138] M. Du, H. Song, Z. Zhang, D. Duan, and T. Cui, Room-temperature superconductivity in Yb/Lu substituted clathrate hexahydrides under moderate pressure, Research **2022**, 9784309 (2023).

[139] W. Zhao, D. Duan, M. Du, X. Yao, Z. Huo, Q. Jiang, and T. Cui, Pressure-induced high-T_c superconductivity in the ternary clathrate system Y-Ca-H, Phys. Rev. B **106**, 014521 (2022).

[140] P. Song, Z. Hou, P. B. de Castro, K. Nakano, K. Hongo, Y. Takano, and R. Maezono, High-T_c superconducting hydrides formed by LaH_{24} and YH_{24} cage structures as basic blocks, Chem. Mater. **33**, 9501 (2021).

[141] X.-L. He, P. Zhang, Y. Ma, H. Li, X. Zhong, Y. Wang, H. Liu, and Y. Ma, Potential high-temperature superconductivity

in the substitutional alloy of (Y, Sr)H_{11} under high pressure, Phys. Rev. B **107**, 134509 (2023).

[142] J. Bi *et al.*, Stabilization of superconductive La–Y alloy superhydride with T_c above 90 K at megabar pressure, Mater. Today Phys. **28**, 100840 (2022).

[143] D. V. Semenok *et al.*, Superconductivity at 253 K in lanthanum–yttrium ternary hydrides, Mater. Today **48**, 18 (2021).

[144] J. Bi, Y. Nakamoto, P. Zhang, K. Shimizu, B. Zou, H. Liu, M. Zhou, G. Liu, H. Wang, and Y. Ma, Giant enhancement of superconducting critical temperature in substitutional alloy (La, Ce)H_9, Nat. Commun. **13**, 5952 (2022).

[145] L.-C. Chen *et al.*, Synthesis and superconductivity in yttrium-cerium hydrides at high pressures, Nat. Commun. **15**, 1809 (2024).

[146] P. Song, A. P. Durajski, Z. Hou, A. Ghaffar, R. Dahule, R. Szczęśniak, K. Hongo, and R. Maezono, (La, Th)H_{10}: Potential high-T_c (242 K) superconductors stabilized thermodynamically below 200 GPa, J. Phys. Chem. C **128**, 2656 (2024).

[147] K. Gao, W. Cui, J. Shi, A. P. Durajski, J. Hao, S. Botti, M. A. L. Marques, and Y. Li, Prediction of high-T_c superconductivity in ternary actinium beryllium hydrides at low pressure, Phys. Rev. B **109**, 014501 (2024).